IJMGE
Int. J. Min. & Geo-Eng.
Vol.49, No.1, June 2015, pp.1-18.

3D Inversion of Magnetic Data through Wavelet based Regularization Method

Maysam Abedi[1*], Hamid-Reza Siahkoohi[2], Ali Gholami[3] and Gholam-Hossain Norouzi[4]

[1] *Department of Mining Engineering, College of Engineering, University of Tehran, Iran, E-mail: maysamabedi@ut.ac.ir*

[2] *Institute of Geophysics, University of Tehran, Iran, E-mail: hamid@ut.ac.ir*

[3] *Institute of Geophysics, University of Tehran, Iran, E-mail: agholami@ut.ac.ir*

[4] *Department of Mining Engineering, College of Engineering, University of Tehran, Iran, E-mail: norouzih@ut.ac.ir*

Received 23 Aug 2014; Received in revised form 10 Apr 2015; Accepted 21 Apr 2015
[*]*Corresponding Author Email: maysamabedi@ut.ac.ir, Tel: +98 9173124132*

Abstract
This study deals with the 3D recovering of magnetic susceptibility model by incorporating the sparsity-based constraints in the inversion algorithm. For this purpose, the area under prospect was divided into a large number of rectangular prisms in a mesh with unknown susceptibilities. Tikhonov cost functions with two sparsity functions were used to recover the smooth parts as well as the sharp boundaries of model parameters. A pre-selected basis namely wavelet can recover the region of smooth behaviour of susceptibility distribution while Haar or finite-difference (FD) domains yield a solution with rough boundaries. Therefore, a regularizer function which can benefit from the advantages of both wavelets and Haar/FD operators in representation of the 3D magnetic susceptibility distributionwas chosen as a candidate for modeling magnetic anomalies. The optimum wavelet and parameter β which controls the weight of the two sparsifying operators were also considered. The algorithm assumed that there was no remanent magnetization and observed that magnetometry data represent only induced magnetization effect. The proposed approach is applied to a noise-corrupted synthetic data in order to demonstrate its suitability for 3D inversion of magnetic data. On obtaining satisfactory results, a case study pertaining to the ground based measurement of magnetic anomaly over a porphyry-Cu deposit located in Kerman province of Iran, Now Chun deposit, was presented to be 3D inverted. The low susceptibility in the constructed model coincides with the known location of copper ore mineralization.

Keywords: *Magnetic anomaly, Sparsity constraints, Wavelet transform, 3D modeling.*

1. Introduction

One of the most important topics in applied geophysics is the inversion of non-unique problems. Inversion of geophysical data is often non-unique meaning that the solution might not depend solely on the data and additional information is required to determine

an appropriate solution. Many attempts have been made in the geophysical context to find a unique and stable solution for geophysical inverse problems suffering from under-determined and instability of solutions [1-4].

Many researchers have studied the inversion of magnetic data to determine the magnetic properties and geometry of subsurface causative sources. Li and Oldenburg (1996) proposed a comprehensive technique for 3D inversion of magnetic data [5]. Their approach is based on the minimization of a global objective function composed of a model regularizer function and a data misfit. They introduced a depth-weighting function to counteract the spatial decay of the kernel function with depth by giving more weight to rectangular prisms as depth increases. Depth weighting has also been applied in other inversion algorithms ([1-2, 6-16]). A comprehensive approach to large-scale magnetic data inversion has also been presented by Li and Oldenburg (2003) [17].

Algorithms based on a smooth model recovering causes a distorted model in regions where sharp discontinuities exist [5-6, 17]. To tackle this limitation, non-linear methods such as edge-preserving techniques have been proposed in various fields including electrical and medical engineering [18-19] and geophysics [14, 20-25]. Edge-preserving inversion is sensitive to the presence of noise in data [3, 18, 26], but appropriately preserves sharp discontinuities in model parameters. Sparsity based inversion is stable against noise [26-30]. It recovers the regions of smooth behaviour properly but leads to some extent smoothed edges and the solution will be oscillatory in the vicinity of sharp discontinuities [3]. Thus, a combination of different regularization methods can be considered to recover model parameters preserved from both smooth and rough boundaries. The sparseness constraints by means of the Cauchy norm have also been applied to model the magnetic data by Pilkington (2009) [6].

In this study sparsity constraints method was implemented as applied by Gholami and Siahkoohi (2010) in seismic data modeling, to invert a model of magnetic susceptibility in copper exploration [3]. Therefore, the commonly wavelet-based sparsity inversion as a smooth edge-preserving technique was added to Tikhonov cost function while both Haar and FD operators were included to preserve the roughness of the recovered solution. In addition, based on the measure of smoothness and roughness of the recovered solution, the optimum wavelet function and parameter β which controls the weight of the sparsifying operators were determined.

To this end, after a brief introduction of inverse procedure, a noisy synthetic multi-source magnetic anomaly was simulated to demonstrate the capability of the applied method. The L-curve as a function of the norm of the regularized solution versus the norm of the data misfit is used as an appropriate method to choose an optimum regularization parameter in magnetic data inversion. In what follows, real data pertaining to the Now Chun porphyry copper deposit located in Kerman, central Iran is presented to be 3D inverted. A comparison with Cu concentration distribution of the Now Chun is also provided.

2. Methodology

To perform inverse modeling, an ensemble of rectangular prisms provides a simple way to approximate a volume of mass. If small enough, each rectangular prism can be assumed to have constant susceptibility. For low susceptibility values, a linear relationship between susceptibility and magnetic anomaly intensity can be assumed; therefore, the inverse problem reduces to solving a linear system of equations [14]. For simplicity, this study assumes that there is no remanent magnetization in modelling and subsequently for such cases the observed data are solely generated by the induced magnetization effects. A comprehensive set of approaches to deal with remanent magnetization has been studied by Lelièvre and Oldenburg (2009) and Li *et al*. (2010) [31-32].

2.1. Forward modeling

Forward modeling of magnetic data were first presented by Bhattacharyya (1964) and later simplified into a form more suitable for fast computer implementation [33-34]. Here, the formulation of Rao and Babu (1991) was used to compute magnetic response of each prism. If the observed anomalies are caused by *m*

prisms, the equation for the magnetic anomaly at the field point (x, y, 0) is given by

$$\Delta T\left(x,y,0\right)=\sum_{r=1}^{m}\Delta T_r\left(x,y,0\right)+C \qquad (1)$$

where ΔT denotes total magnetic observation and C represents a regional constant [34]. In the matrix notation, considering that there are n observed field data and m rectangular prisms, Equation (1) can be written as

$$T_{n\times 1}=G_{n\times m}X_{m\times 1} \qquad (2)$$

where $\boldsymbol{T}$ is the data vector (residual magnetic data by removing the constant $\boldsymbol{C}$), $\boldsymbol{G}$ is the forward operator matrix that maps from the physical parameter space to the data space, and X is the unknown model parameter vector containing susceptibility of the prisms.

2.2. Inverse Modeling

The linear operator **G** has a multidimensional null-space. Indeed, the solution has to be regularized [4]. It is supposed that data are contaminated with white Gaussian noise of zero mean and finite variance σ^2. The unknown susceptibility vector can be estimated by optimizing a multi-term cost function as,

$$f\left(X_{opt}\right)=\min_X\left\{\left\|T-GX\right\|_2^2+\alpha\left[(1-\beta)\sum_i\left|\left[S_1X\right]_i\right|+\beta\sum_i\left|\left[S_1X\right]_i\right|\right\}\right. \qquad (3)$$

Here, $\alpha>0$ and $0\le\beta\le1$ are regularization parameter. The parameter β controls the relative weight of the two sparsity terms S_1 and S_2 which are two suitable sparsifying operarors. The sparsifying operators were firstly applied by Gholami and Siahkoohi (2010) to inverse seismic traveltime tomography while they attempted to recover model parameters preserving both smoothness and roughness [3]. The operator S_1 is chosen as a suitable wavelet operator which provide sparse representation of geological models. The wavelet transform expands a function on the bases formed by the translation and dilation of a single function called the mother wavelet. Let $y(x)$ be the function and $\psi(x)$ be the mother wavelet. Then the wavelet transform $\omega(a, b)$ is defined by

$$\omega\left(a,b\right)=\int_{-\infty}^{+\infty}y\left(x\right)\psi_{a,b}\left(x\right)dx \qquad (4)$$

where

$$\psi_{a,b}\left(x\right)=\frac{1}{\sqrt{a}}\psi\left(\frac{x-b}{a}\right) \qquad (5)$$

and a and b are the dilation and translation variables, respectively. The wavelet transform $\omega(a, b)$ describes the frequency or scale content (measured by a) at different locations (measured by b), that is, it provides resolution in both the spatial and frequency domains. For practical applications, the dilation and translation variables have a set of discrete values which are typically dyadic. The wavelet is then expressed as a double-indexed function,

$$\psi_{j,d}\left(x\right)=2^{-j/2}\psi\left(2^{-j/2}x-d\right) \qquad (6)$$

where j and d are integers. A class of wavelets are constructed by solving the two-scale difference equation,

$$\phi\left(x\right)=\sqrt{2}\sum_{d=0}^{K-1}h_d\phi\left(2x-d\right) \qquad (7)$$

$$\psi\left(x\right)=\sqrt{2}\sum_{d=0}^{K-1}g_d\phi\left(2x-d\right) \qquad (8)$$

where ϕ is the scaling function. The wavelet $\psi\left(x\right)$ is defined by a set of filter coefficients h_d and g_d called the quadrature mirror filters. Daubechies (1988) constructed a class of such wavelets that has several important properties [35]. These wavelets are orthogonal to the dyadic translation and dilation of the original version, have compact support,are localized both in space and in frequency domain and are constructed to have M vanishing moment:

$$\int_{-\infty}^{+\infty}\psi\left(x\right)x^m dx=0\ ,\ m=0,...,M-1 \qquad (9)$$

where M is an integer. When $M=1$, the Haar wavelet is obtained and when $M=2$, Daubechies-4 (db4) wavelet defined by a quadrature mirror filter of length 4 is obtained. As an illustration, both wavelets are shown in Figure 1 [17].

In addition, the operator S_2 as one of the Haar or FD operators provides sparse representation of models not suffering from smoothed edges and the pseudo-Gibbs phenomenon. These operators are referred to as roughening matrices with discrete χ for the purposes of regularization and could effectively

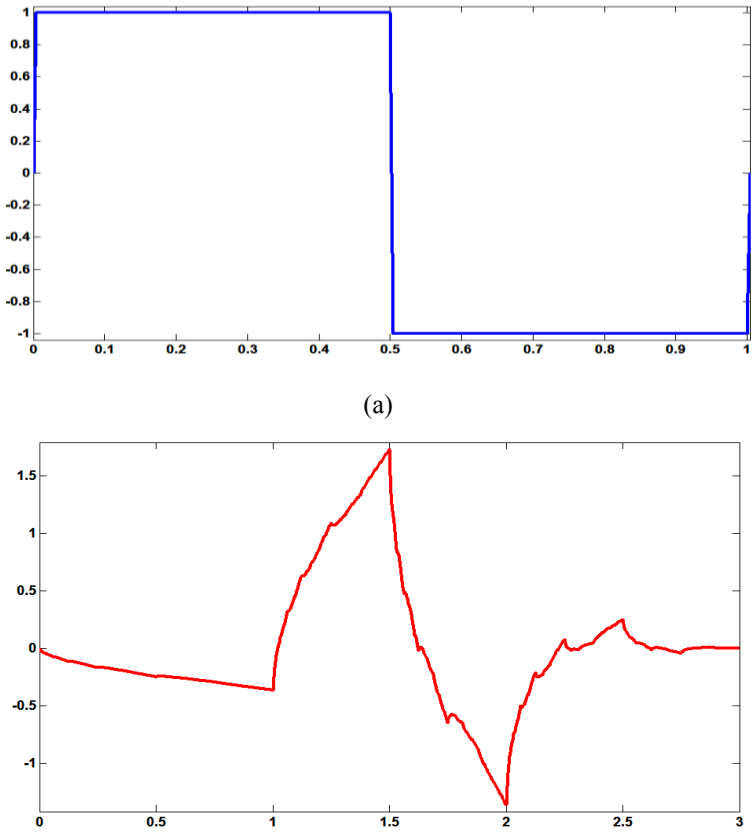

Fig. 1. Wavelet-basis operators, (a) the Haar wavelet which has 1 *vm*, (b) the db4 wavelet with 2 *vm*

retrieve sharp boundaries of model parameters χ by providing sparse representation of the model. For instance $S_2\chi$ when operator corresponds to FD is a finite-difference approximation that is proportional to the first derivative of χ. By minimizing $\left|\left[S_2 X\right]_i\right|$, it would be favor solutions that are relatively sharp. Consequently, by imposing sparsity constraints jointly on magnetic data in such domains, this study aims to combine the advantages of both operators to obtain high-resolution solution of susceptibilities distribution in magnetic prospect. Interested readers are referred to Aster *et al*. (2003) for further information about constructing a FD operator in 1D, 2D and 3D domains. The wavelet transform of geological models is generally sparse with many small coefficients; therefore, the sparsity regularization will remove small coefficients based on the amount of regularization parameter α which is determined by L-curve method in this study. This results in smooth edges and put some oscillations near the discontinuities of the final solution. It is assigned a non-zero value for β, $0<\beta<1$, to enforce the model to be jointly sparse in the domain defined by S_2. This will typically recover small coefficients to eliminate such ripples while preserving edges. This arises from the fact that S_2 does provide sparse representations of models without generating smoothed edges and the pseudo-Gibbs phenomenon.

Magnetic data have no inherent depth resolution. As a result, structures tend to concentrate near the surface when a simple model is produced, regardless of the true depth of the causative magnetic anomaly sources. In terms of model construction, the kernel function decreases with depth so that surface data are not sufficient to generate significant structures at depth. To overcome this lack of sensitivity in magnetic data inversion, depth weighting has been introduced by Li and

Oldenburg (1996) to cancel the natural decay and give cells at different depths equal probability of entering the solution with a non-zero susceptibility value [5, 15]. The proposed depth weighting function is of the form

$$W(z)=(z+\epsilon)^{-\mu}$$

where μ is close to 1.5 and ϵ depends on the observation of height level. The parameter ϵ can be selected equal to a small value to prevent singularity when z is close to 0 [10]. The calculated depth weighting coefficients make the diagonals of a matrix $Z=diag(W(z))$ to be introduced to the original system of equations (3) by setting $G_z=GZ^{-1}$ and $k=ZX$ and solving the problem for k. After this procedure, the final susceptibility model is obtained as $X=Z^{-1}k$ [17]. The split Bregman technique described in the following section is used to solve equation (3).

2.3. Solution by the split Bregman method

The Bregman splitting method, which is derived using Bregman distance, is very efficient in terms of convergence and numerical stabilities [37]. Equation (3) in terms of matrix representation is calculated,

$$\chi^{k+1}=\left(G^{T}G+\gamma S_1^{T}S_1+\lambda S_2^{T}S_2\right)^{-1}\left(G^{T}T+\gamma S_1^{T}\left(p_1^{k}-q_1^{k}\right)+\lambda S_2^{T}\left(p_2^{k}-q_2^{k}\right)\right) \quad (10)$$

Parameters γ and λ are positive numbers which are the split parameters, and X^{k+1} is the constructed model parameters at iteration $k+1$ which is uniquely determined from the vectors p_i^k , q_i^k , where $i=1,2$. The algorithm is started by setting $p_i^0=q_i^0=0$, then at the next iterations they are constructed from the solution of L1-norm subproblems computed easily using shrinkage operators applied on the coefficients of X^{k+1}. For the computations of p_i and q_i, we refer to Bregman splitting algorithm summarized in Table 1 for more details. In the algorithm, $shrink(x,\tau)$ is the so-called soft thresholding operation [38];

$$shrink(x,\tau)=\begin{cases}x-\tau & x>\tau\\ 0 & |x|\le\tau\\ x+\tau & x<-\tau\end{cases} \quad (11)$$

Table 1. The Bregman splitting algorithm for minimization of the cost function $f(\chi_{opt})$ in equation 3 [3]

Chose	ε,λ *and* γ
Set:	$\tau_1=\gamma^{-1}\alpha(1-\beta),\ \tau_2=\lambda^{-1}\alpha\beta$
	$\mathbf{B}=\mathbf{G}^{T}\mathbf{G}+\gamma\mathbf{I}+\lambda\mathbf{S}_2^{T}\mathbf{S}_2$
Initialize	$\chi^0=\mathbf{G}^{T}\mathbf{d};\quad \mathbf{p}_1^0=\mathbf{p}_2^0=\mathbf{q}_1^0=\mathbf{q}_2^0=0;$
	$k=0;$
While	$\dfrac{\chi^{k}-\chi^{k-1}}{\chi^{k}}>\varepsilon$
$\chi^{k+1}=\mathbf{B}^{-1}\left\{\mathbf{G}^{T}\mathbf{T}+\gamma\mathbf{S}_1^{T}\left(\mathbf{p}_1^{k}-\mathbf{q}_1^{k}\right)+\lambda\mathbf{S}_2^{T}\left(\mathbf{p}_2^{k}-\mathbf{q}_2^{k}\right)\right\}$	
$\mathbf{c}_1^{k+1}=\mathbf{S}_1\chi^{k+1}+\mathbf{q}_1^{k}$	
$\mathbf{c}_2^{k+1}=\mathbf{S}_2\chi^{k+1}+\mathbf{q}_2^{k}$	
$\mathbf{p}_1^{k+1}=\text{shrink}\left(\mathbf{c}_1^{k+1},\tau_1\right)$	
$\mathbf{p}_2^{k+1}=\text{shrink}\left(\mathbf{c}_2^{k+1},\tau_2\right)$	
$\mathbf{q}_1^{k+1}=\mathbf{c}_1^{k+1}-\mathbf{p}_1^{k+1}$	
$\mathbf{q}_2^{k+1}=\mathbf{c}_2^{k+1}-\mathbf{p}_2^{k+1}$	
$k=k+1;$	
End	

The computational cost of the algorithm is largely depended on how fast the system of equation (10) can be solved, the application of the sparsifying operators, and their transposes. In the case of transformation operators with $S^T Sx = \mathrm{I}x$, the application of operator and its transpose simply are the discrete decomposition and reconstruction schemes [3]. When S_2 is the Haar operator, the left-hand side matrix reduces to $\mathrm{B} = \mathrm{G}^{\mathrm{T}}\mathrm{G} + (\gamma + \lambda)\mathrm{I}$ and when it is FD operator $\mathrm{B} = \mathrm{G}^{\mathrm{T}}\mathrm{G} + \gamma\mathrm{I} + \lambda\Delta$, where I is the identity matrix and $\Delta = \mathrm{S}_2^{\mathrm{T}}\mathrm{S}_2$ is a sparse matrix.

In the case of large-scale problems, it is difficult to explicitly solve the central system of Equation (10) using direct solvers; instead, iterative methods such as conjugate gradients (CG) algorithm can be used to solve it approximately. The convergence rate of CG algorithm can be improved by using pre-conditioner. Preconditioning is a procedure to incorporate a transformation in mathematics, that is, the preconditioner, by which a problem changes into a form that is more suitable to be solved using variety of numerical methods. Preconditioning mostly correspond to reducing a condition number of the preconditioned problem which is then usually solved by iterative methods. The Jacobi preconditioner is one of the simplest and prevalent forms of preconditioning, in which the preconditioner is chosen to be the diagonal of the desired matrix. It only increases the speed of convergence to the final solution. Li and Oldenburg (2003) have used a Jacobi-like pre-conditioner to treat large scale data [17]. In this paper, a diagonal pre-conditioner is used [14]. Thus, when S_2 is Haar operator, the diagonal pre-conditioner M is

$$\mathrm{M} = \mathrm{diag}\left(\mathrm{G}^{\mathrm{T}}\mathrm{G} + (\gamma + \lambda)\mathrm{I}\right) = \mathrm{diag}(\mathrm{A}) \qquad (12)$$

and when S_2 is FD operator, M is

$$\mathrm{M} = \mathrm{diag}\left(\mathrm{G}^{\mathrm{T}}\mathrm{G} + \gamma\mathrm{I} + \lambda\Delta\right) = \mathrm{diag}(\mathrm{A}) \qquad (13)$$

where $diag(\mathrm{A})$ is calculated by setting off-diagonal elements of matrix *A* to zero. The total number of iterations and the running time of algorithm depend on parameters γ and λ. In this study, we choose $\gamma = \lambda = \sigma_{max}$, where σ_{max} is the largest singular value of the forward operator *G*. It is found that this assumption results to reasonable convergence of both CG and split Bregman method.

2.4. Optimal selection of wavelet function and regularization parameters

The main goal of joint-sparsity constraints is to recover the smooth and rough edges of model parameters. Both wavelet function and β impact on the performance of the joint-sparsity regularizer function and must be chosen appropriately. Optimal value of β chosen at an interval $0 \le \beta \le 1$ balances the effect of the two constraints to recover the smooth as well as the rough part of the model parameters. Generally, the wavelet operator, which leads to the orthonormal wavelet operator S_1, should provide a sparse coefficient vector [39-40]. Therefore, the recovered model can be considered as a function of β and wavelet function [3].

A function considered by Gholami and Siahkoohi (2010) is used to determine optimal parameters for joint-sparsity constraints. It used the L2-norm of the second derivative of the regularized solution, $\left\|\mathrm{D}^{(2)}\chi(\beta, \mathrm{vm})_2\right\|$ as a measure of smoothness and L1-norm of its first derivative, $\left\|\mathrm{D}^{(1)}\chi(\beta, \mathrm{vm})_1\right\|$ as a measure of roughness (where $\mathrm{D}^{(\mathrm{i})}$ is the *i*th-order derivative operator), and defined an information function as follows;

$$\mathrm{I}(\beta, \mathrm{vm}) = \left\|\mathrm{D}^{(1)}\chi(\beta, \mathrm{vm})_1\right\| + \left\|\mathrm{D}^{(2)}\chi(\beta, \mathrm{vm})_2\right\| \qquad (14)$$

where *vm* is the vanishing moments of Daubechies wavelets. The main advantage of this information function is that the algorithm does not need to the true model (χ_{real}), especially when real data inversion is being studied. The selected β and *vm* should minimize $I(\beta, vm)$. The applicability of this function is compared to the result norm of model error $\left\|\chi(\beta, \mathrm{vm}) - \chi_{\mathrm{real2}}\right\|$ in synthetic data inverse problem to evaluate its performance. It is shown that the information function can be a good method for choosing optimum β and *vm* in case of real data inversion when we have no access to of χ_{real} values.

3. Application to the synthetic data

To evaluate the capability of the proposed method in magnetic data modeling, a synthetic

magnetic anomaly consisting of two different bodies involving a step-shape and a block model is simulated with susceptibility values of 0.08 and 0.1 in SI unit, respectively (Figs. 2 and 7a). A non-susceptible background is considered. The 3D domain is divided into $32\times32\times32=32768$ prisms with dimension $25\times25\times12.5$ m. The inducing magnetic field has direction $I=50^{\circ}$, $D=2^{\circ}$ and a strength of $47,000nT$. Residual magnetic field is shown in Figure 3a. Random Gaussian noise with a standard deviation of 3% of the data amplitude has been added to the data. It consists of 1024 data points over a grid of 800×800 m spacing to implement inverse approach.

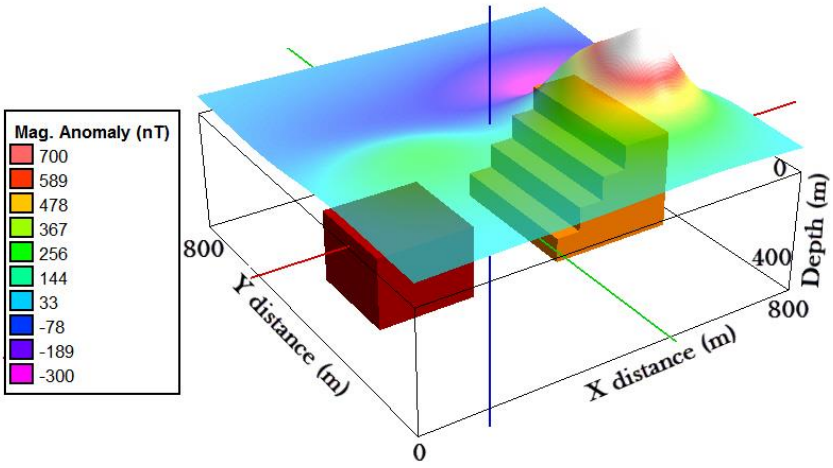

Fig. 2. 3D visualization of the synthetic magnetic sources comprising of two separated anomalies

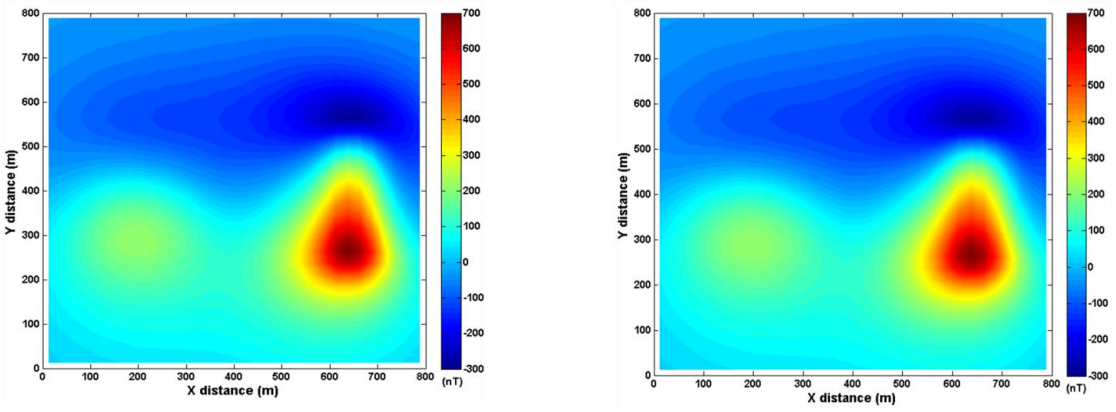

(a) (b)

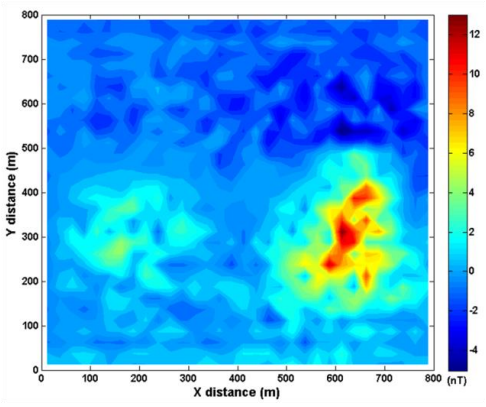

(c)

Fig. 3. Synthetic data modeling, a) the synthetic magnetic data to be inverted, b) the predicted response from the inverted model, and c) the residual magnetic data that show the difference between the predicted and the observed data

The parameters β and vm should be optimized to plot 3D distribution of susceptibility model. To select the optimum wavelet function and β, the data set by joint-sparsity inversion was inverted using different choices of vanishing moment and $0 \le \beta \le 1$ with small increments of β. Then both information function and model error as a function of β and increasing orders of the vanishing moments of the wavelet function were plotted. The results of S_2 as Haar and FD operators are shown in top and bottom rows of Figure 4, respectively. In the lower panels, the information function considering the FD operators causes lower values compared to the Haar operator. The rectangular areas for both the information function and the model error function provide acceptable values of the β and vm . It shows that the information function causes similar results like the model error function and it can be used in real data inversion. Since the FD operator provides lower error, 3D inversion of magnetic data considering this operator is applied. The *db7* wavelet with $\beta = 0.3$ are chosen as appropriate values to this aim. The optimum value of the regularization parameter $\alpha = 2000$ was acquired from L-curve plot (Fig. 5) in which the curvature attains to a maximum value at this amount. Figure 6 shows the results of the method for four different depth levels of 75, 125, 175 and 225m, respectively. As shown, multi-source location is reported to be properly associated with locations of synthetic rectangular bodies. The predicted magnetic anomalies of synthetic example shown in Figure 3b are acceptably close to synthetic magnetic data. A residual map of the predicted and real magnetic data shown in Figure 3c also confirms low misfit data of the 3D model.

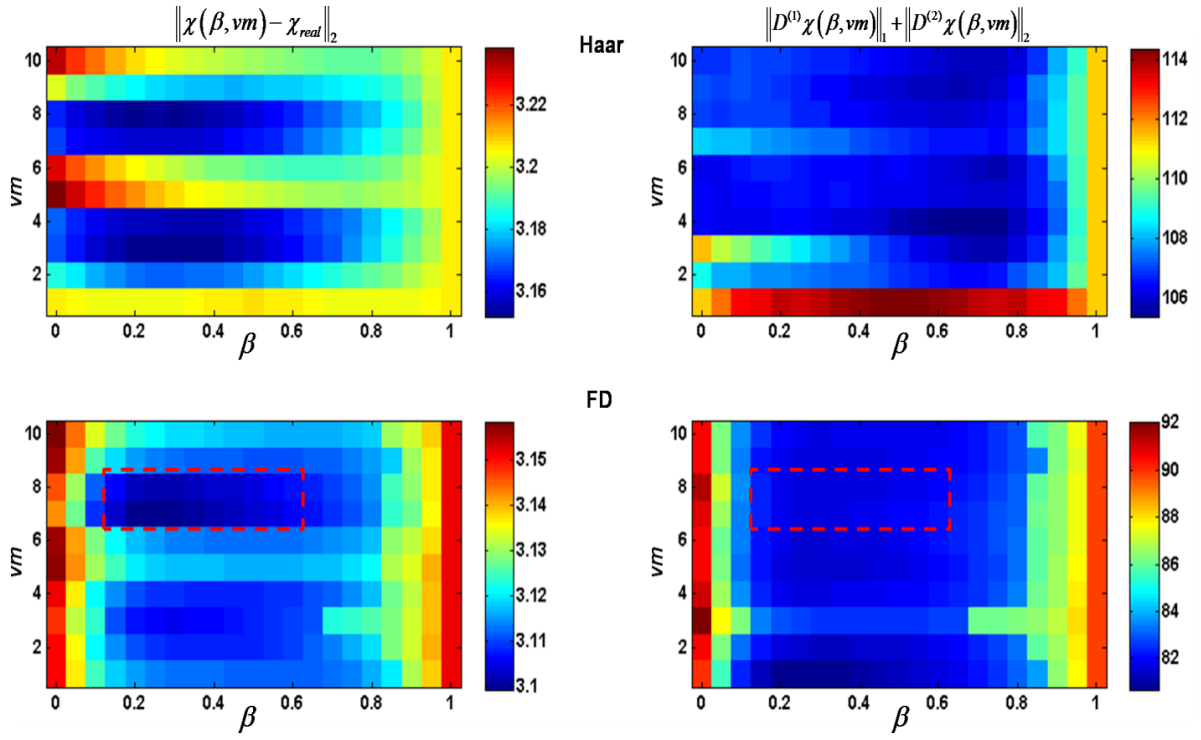

Fig. 4. Maps of the norm of model error $\|\chi(\beta,vm)-\chi_{real\,2}\|$ (left-hand column) and information function $\|D^{(1)}\chi(\beta,vm)_1\|+\|D^{(2)}\chi(\beta,vm)_2\|$ (right-hand column) for inverted model from joint-sparsity inversion using Haar (top row) and FD (bottom row) operators. In the panels, the information function considering the FD operators causes lower values compared to the Haar operator. The rectangular areas for both the information function and the model error function provide acceptable values of β and *vm*.

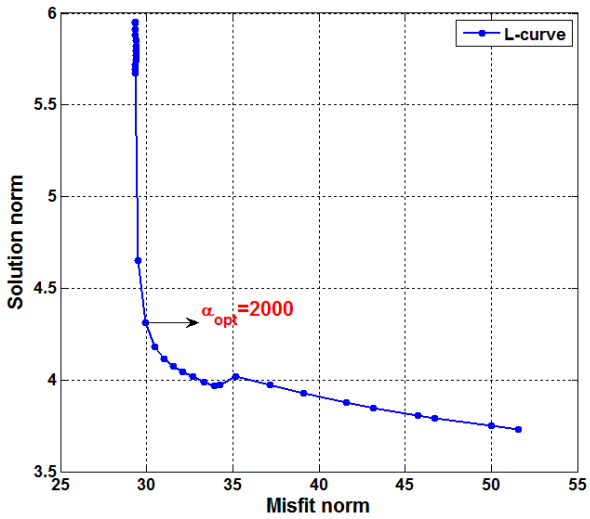

Fig. 5. L-curve plot of synthetic magnetic data by joint-sparsity method assuming the FD operator in the inversion algorithm. Here, the misfit norm ($\left\|T-G.\chi_2^2\right\|$) versus the solution norm ($(1-\beta)\sum_i\left[S_1\chi\right]_i\left|+\beta\sum_i\left[S_2\chi\right]_i\right|$) of Eq. 3 has been plotted.

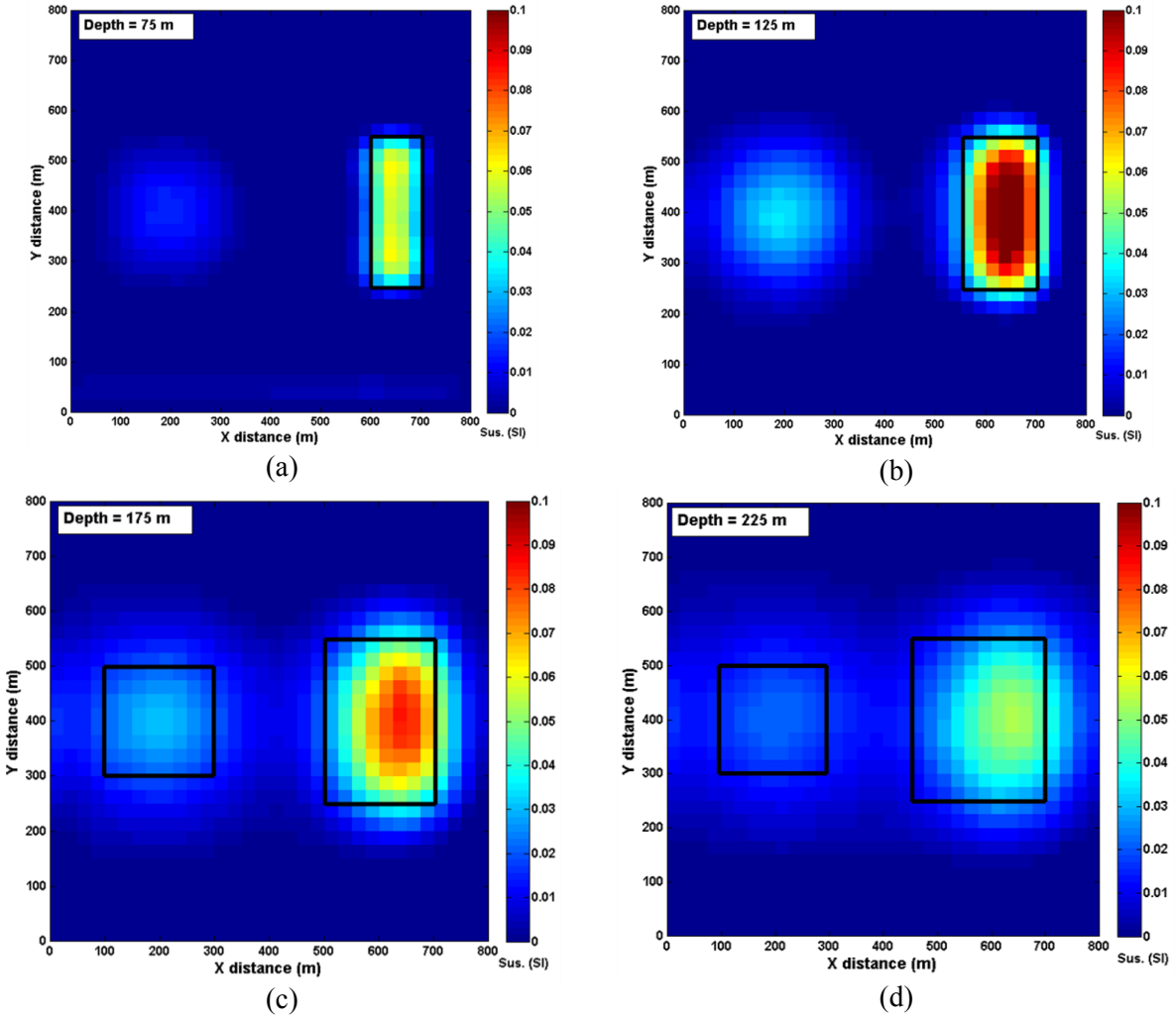

Fig. 6. The inversion results obtained from synthetic data. Horizontal location at (a) depth 75 m, (b) depth 125 m, (c) depth 175 m, (d) depth 225 m. The rectangular borders indicate real location of synthetic models at each plan-section.

Inversion results along *x* direction at Y=400 is shown in Figure 7b. Compared to real sources (Fig. 7a), satisfactory results are acquired. The point to be considered in 3D inversion of magnetic data is that recovering the dipping structure by use of solely surface magnetic data is an under tackling issue in magnetic inverse problem. To recover dipping structures in potential method prospect, boreholes magnetic data also have significant impact on improving inverse problems [10, 41]. Another point is that the depth weighting function by Li and Oldenburg (1996) assumes a sphere model structural index, i.e. $\mu=1.5$. Indeed, this depth weighting function tends to recover a sphere model. It recommended using appropriate values of the structural index to recover proper models. Interested readers are referred to a paper by Cella and Fedi (2012) for using the structural index as weighting function [16]. In summary, two factors including boreholes data and appropriate value of the structural index can increase the resolution of recovered susceptibility model. The authors have no access to borehole magnetic data to implement them in the inversion algorithm.

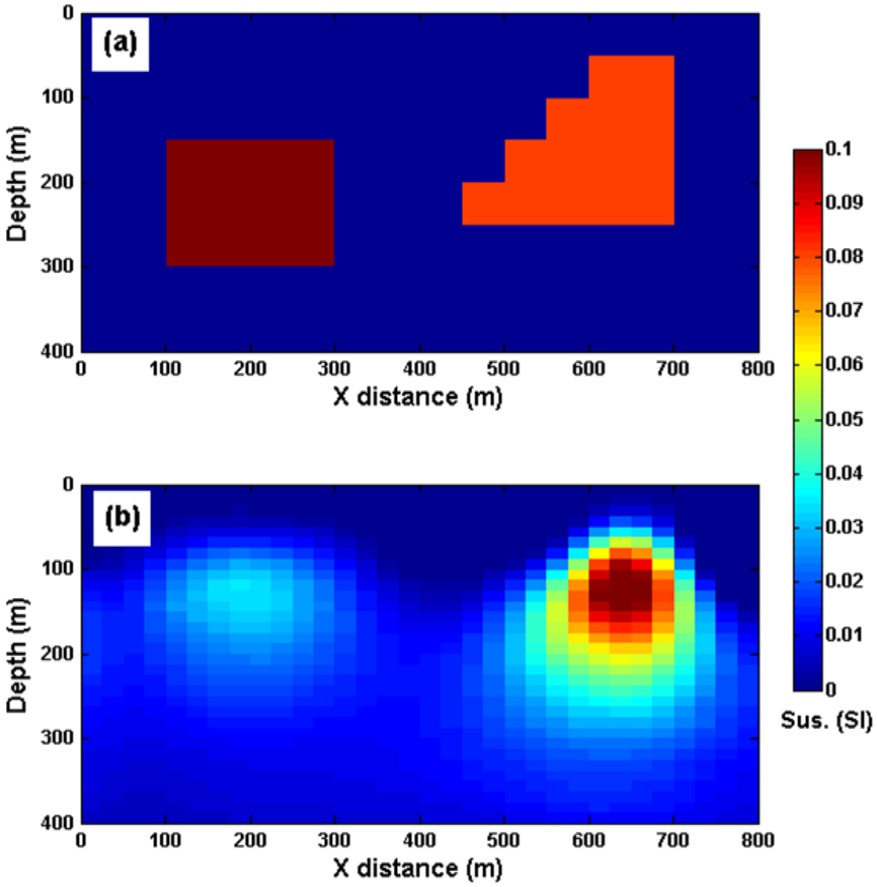

Fig. 7. A cross section view of inverted synthetic magnetic susceptibility at Y= 400 m. a) Real locations of two synthetic bodies, and b) Sparsity-based inversion of magnetic data using depth weighting function by Li and Oldenburg (1996)

4. Geological background of the study area

The case study is located within the Urumieh-Dokhtar (Sahand-Bazman) magmatic arc subdivision of the Central Iran zone where extensive Tertiary to Plio-Quaternary extrusive and intrusive units are exposed in a NW-SE trend (Fig. 8). In general, the main lithological units exposed in the Now Chun area comprise of volcanic-subvolcanic complexes and intrusive bodies. Volcanic rocks cover most parts of the study area and consist of Eocene and esitic, dacitic to rhyo-dacitic lavas and associated breccias tuffs. The intrusive bodies consist of granite to diorite distributed in the South to Southwest of the area [42].

Most of the geological units have been altered hydrothermally with the most intensive alteration occurring in the subvolcanic rhyo-dacitic bodies. The general trend of altered rhyo-dacitic units and hydrothermal dissemination is Northeast-southwest [42]. Since there is comprehensive correlation between hydrothermal zones and faults, it is assumed that alteration zones are controlled by major faults and fractures. However, Cu-bearing mineralization zones are mainly associated with azurite and malachite stockwork veins with minor chalcopyrite as inclusions within quartz. Some copper mineralized outcrops are also shown on the detailed geological map (Fig. 8).

The primary control of the bulk magnetic properties of the host rock and magnetic intrusions is the partitioning of iron between oxides and silicates [43]. However, sulphide minerals associated with hydrothermal alteration also provide localized geophysical targets [44]. Simple models for porphyry-Cu deposits involve contrasting zones of alteration centered on the deposit. Magnetic anomalies, at least in principle, reflect the location of these zones: weak local magnetic highs occur over the potassic zone; low magnetic intensity occurs over the sericitic zones; and magnetic intensities increase gradually over the propylitic zone [45]. Inversion of magnetic data has also been used to model a copper gold porphyry deposit at Mt. Milligan with satisfactory comparison between constructed susceptibility model and known anomaly source [46].

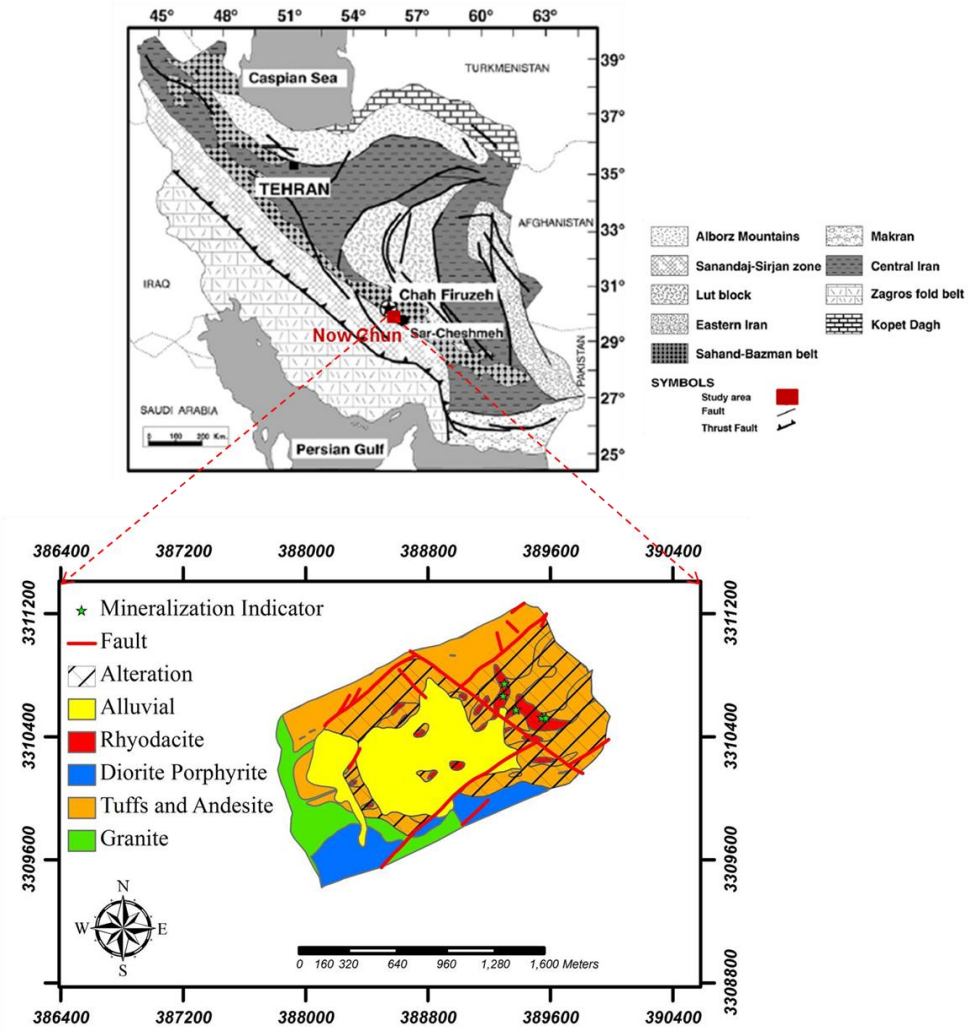

Fig. 8. Detailed geological and mineral occurrence map of Now Chun copper deposit located in Kerman province of Iran with scale 1:5,000 (reproduced from [42, 48])

5. Real data inversion

A ground-based magnetic survey was performed in the area in which the distances between profiles and stations were 50 and 20 m, respectively. The geomagnetic field is 46,000 *nT* (inclination= 46° and declination= 2.5° from IGRF). After removing the effect of the regional geomagnetic field based on the surface data, residual magnetic data are shown in Figure 9a. The study area was divided into $32\times32\times32=32768$ rectangular prisms with dimensions $41\times31\times19$ *m*. The total number of data points was 1235. Analysis of various porphyry deposits indicates that susceptibility values vary over interval (0.0002, 0.2) in SI unit with an average of 0.06 [47]. Since the average value of susceptibility in porphyry deposit prospects is low, a linear magnetic equation can be used in the inverse problem.

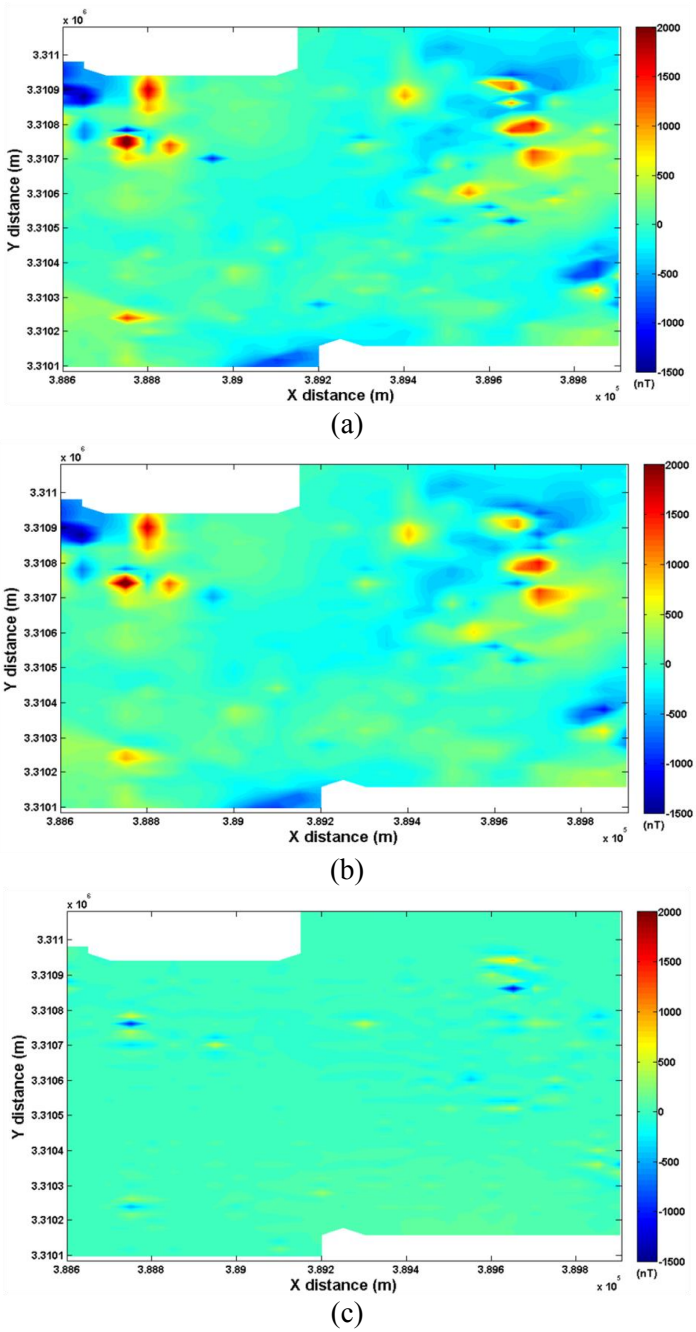

Fig. 9. The anomalous magnetic data modeling at Now Chun porphyry copper deposit, a) the real magnetic data from the field observation, b) the predicted responses from the inverted model, and c) the residual magnetic data which shows difference between the predicted and the observed data

The information function plot of both the Haar and the FD operators result in lower error values of the FD operator shown in Figure 10. Therefore, the FD operator, *db5* wavelet and β=0.95 are chosen as appropriate values to invert real magnetic data. The optimum value of the regularization parameter α=20000 was acquired from L-curve plot shown in Figure 11 to be considered as an appropriate value in the inversion algorithm. Figure 12 shows the 3D plot of the susceptibility distribution for a cut off value of 0.015 in SI. Figure 9b shows the data prediction for the real data inversion and the predicted data compared well with the observed magnetic anomaly shown in Figure 9a. A residual map shown in Figure 9c indicates the insignificant differences. Magnetic susceptibility values acquired from inversion shown in Figure 13 (histogram map) indicates that most values are less than 0.06 in SI unit (M+3SD=0.06) which is well in agreement with the values of porphyry deposits at 0.0002-0.2 interval.

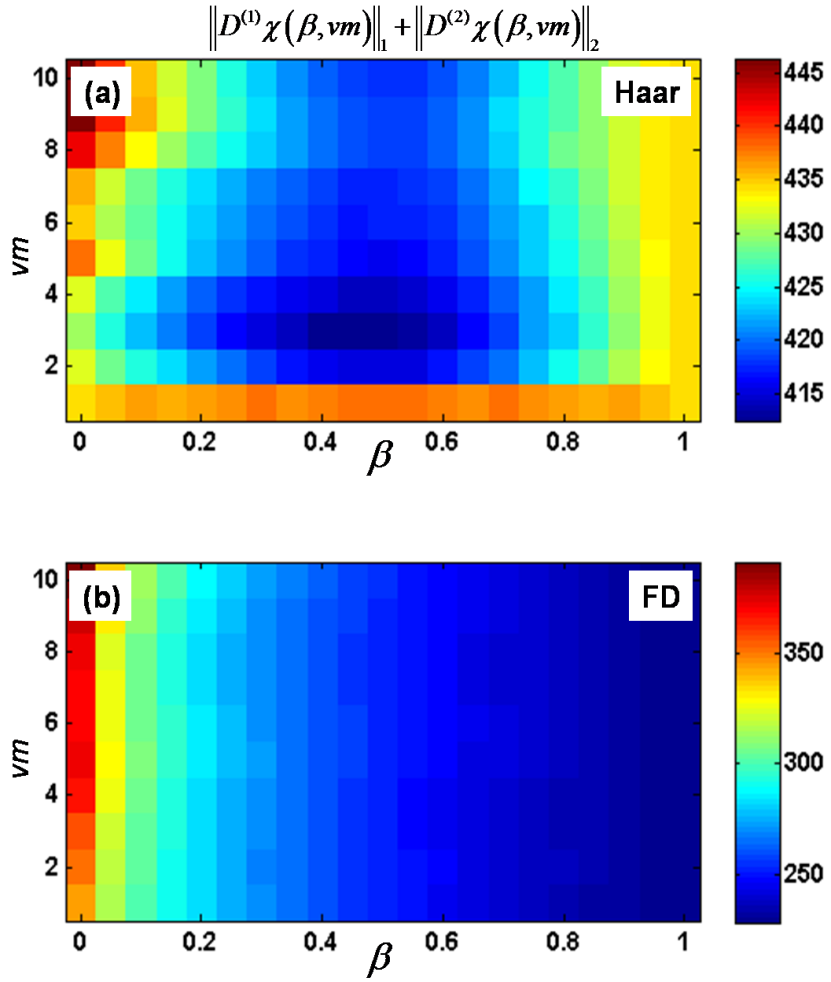

Fig. 10. Maps of the information function $\left\|D^{(1)}\chi(\beta,vm)_1\right\|+\left\|D^{(2)}\chi(\beta,vm)_2\right\|$ for inverting real data by joint-sparsity method, a) using Haar operator, b) using FD operator. The FD operator which causes lower values of the information function is selected as S_2 operator

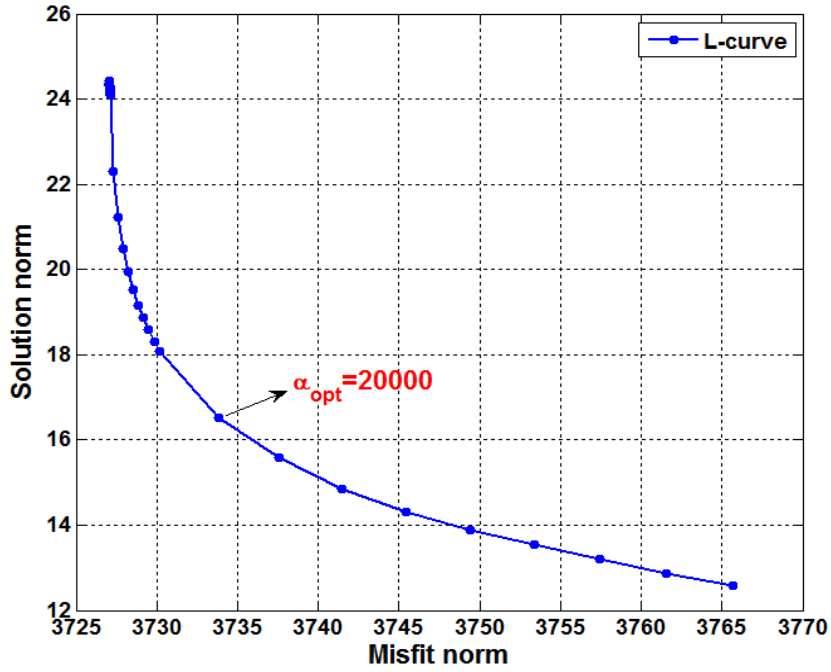

Fig. 11. L-curve plot of real magnetic data by joint-sparsity method assuming the FD operator in the inversion algorithm. Here, the misfit norm ($\left\|T-G.\chi_2^2\right\|$) versus the solution norm ($(1-\beta)\sum_i\left[S_1\chi\right]_1+\beta\sum_i\left[S_2\chi\right]_1$) of Eq. 3 has been plotted.

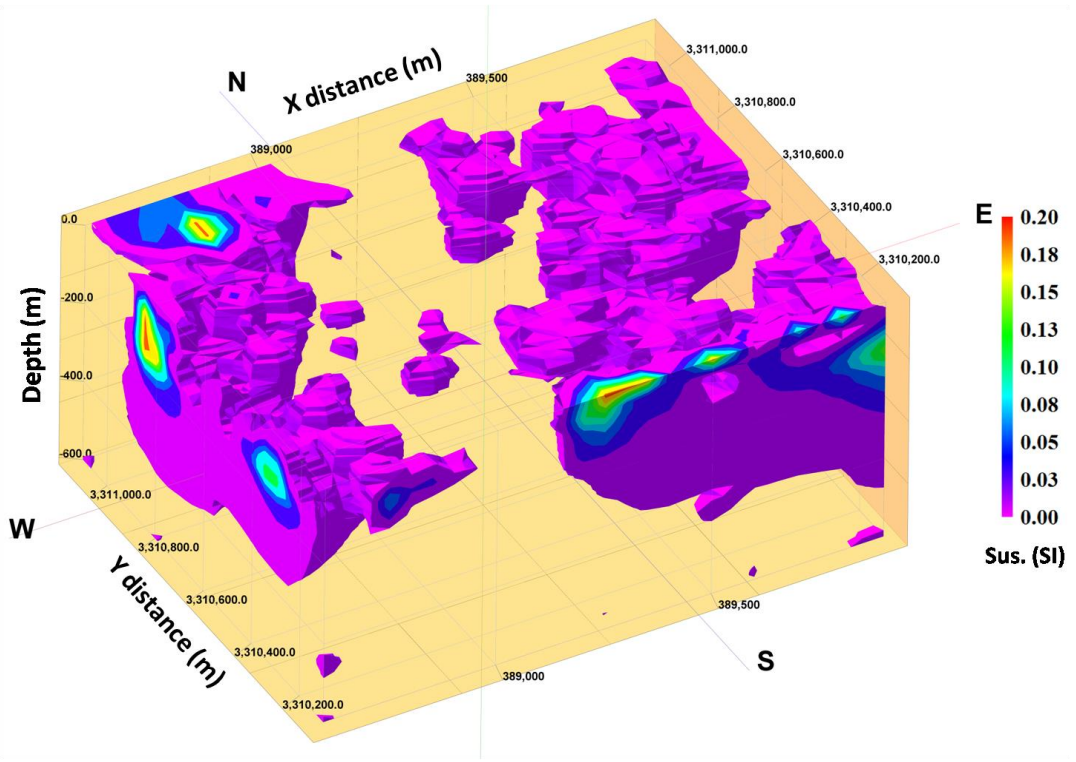

Fig. 12. 3D view of magnetic susceptibility model for Now Chun copper deposit (a cut off value of 0.015 SI)

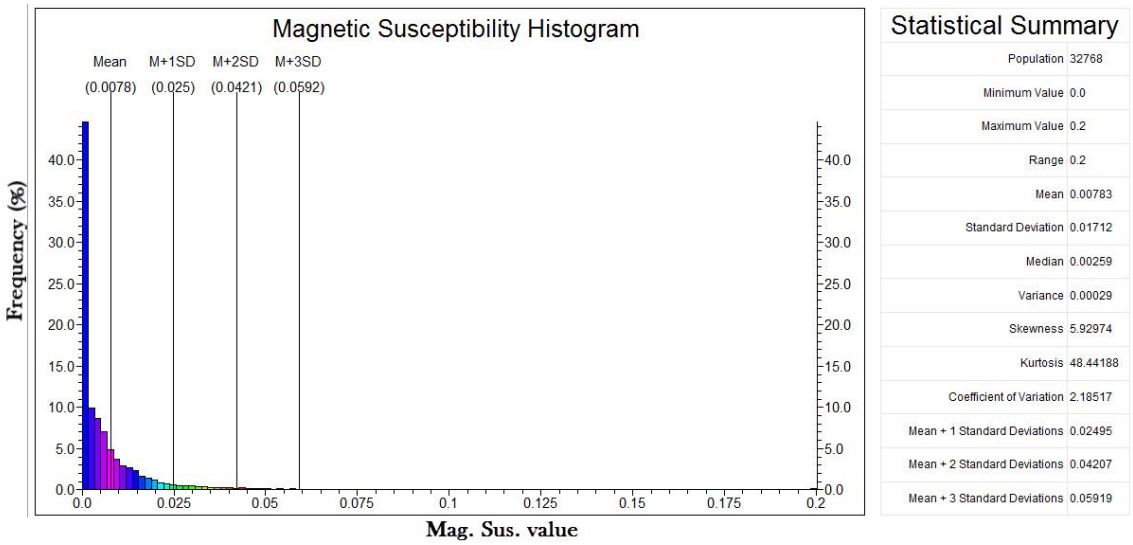

Fig. 13. Histogram of the magnetic susceptibility values with its statistical summary

The 3D view of Cu concentration for an economical cut off of 0.3 % is shown in Figure 14. Compared to the 3D susceptibility model shown in Figure 12, it indicates that higher values of Cu concentration correspond to lower values of the susceptibility model. The main part of Cu mineralization is surrounded by high magnetic anomalies, that is higher values of susceptibilities. Indeed, it reflects the effect of propylitic alteration which is around the main mineralization source. It shows that low magnetic susceptibilities at Now Chun deposit contain mainly Cu distribution. Since sericitic alteration depletes magnetite content, it yields low magnetic anomaly over this zone.

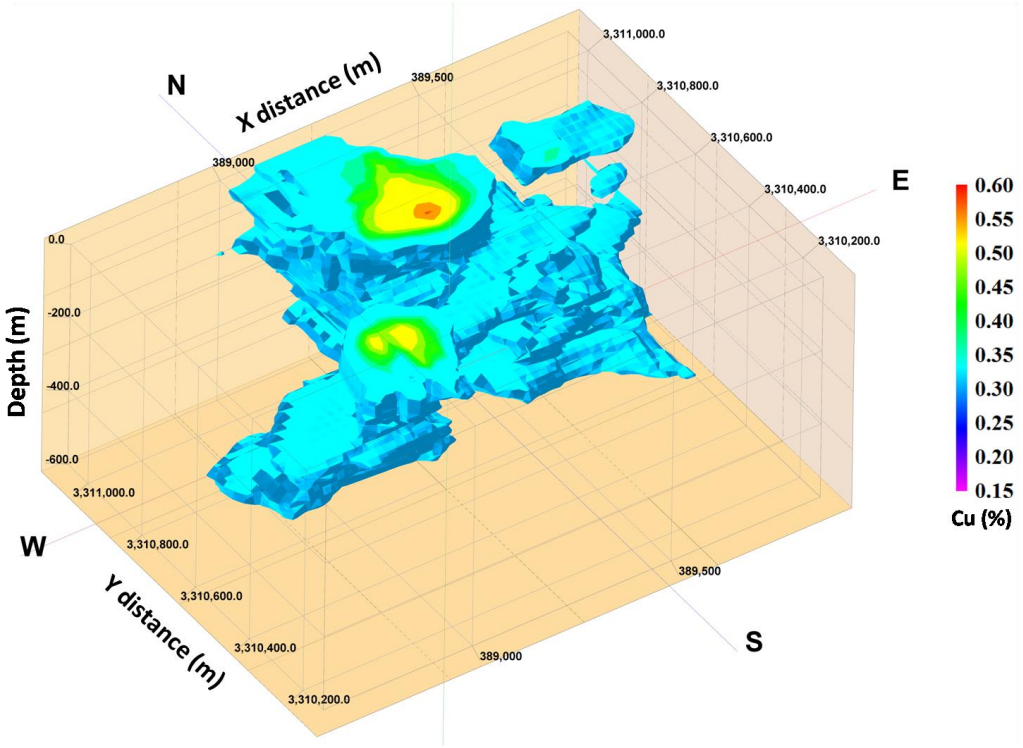

Fig. 14. 3D view of Cu concentration for an economical cut off 0.3%

6. Conclusion

This study presents an efficient algorithm for 3D inversion of magnetic data over a porphyry-Cu deposit located in Kerman Province of Iran. The main characteristic of this study is the implementation of joint-sparsity constraints for simultaneously preserving smooth and rough edges of model parameters. The Daubechies wavelets and the finite difference (FD) operator were used as appropriate prior information to recover magnetic susceptibility model. An interesting result from this study was obtained by comparison of the 3D magnetic susceptibility model to the Cu concentration distribution. It showed that the higher Cu concentration zone corresponded to the lower magnetic susceptibility in the recovered model. It is clearly in agreement with sericitic alteration which shows a high potential for Cu ore body occurrences with geochemically depleted Fe-bearing minerals like magnetite ore (that is low magnetic anomaly).

Acknowledgements

The authors gratefully acknowledge the support provided by the faculty of Mining Engineering, University of Tehran. We also thank the National Iranian Copper Industries Company for their expert opinions and data preparation. We would like to express our sincere thanks to two respectful anonymous referees for their constructive comments which helped us to improve the quality of this research work.

Reference

[1] Abedi, M., Gholami, A., Norouzi, G.H. and Fathianpour, N. (2013). "Fast inversion of magnetic data using Lanczos bidiagonalization method." Journal of Applied Geophysics, Vol. 90, PP. 126-137.

[2] Abedi, M., Gholami, A. and Norouzi, G.H. (2014). "3D inversion of magnetic data seeking sharp boundaries: a case study for a porphyry copper deposit from Now Chun in central Iran." Near Surface Geophysics, Vol. 12, PP. 657-666.

[3] Gholami, A. and Siahkoohi, H.R. (2010). "Regularization of linear and non-linear geophysical ill-posed problems with joint sparsity constraints." Geophysical Journal International, Vol. 180, No. 2, PP. 871-882.

[4] Tikhonov, A.N. and Arsenin, V.Y. (1977). "Solutions of Ill-Posed Problems." Winston, Washington, D.C.

[5] Li. Y. and Oldenburg, D.W. (1996). "3-D inversion of magnetic data." Geophysics, Vol. 61, PP. 394–408.

[6] Pilkington, M. (2009). "3D magnetic data-space inversion with sparseness constraints." Geophysics, Vol. 74, PP. L7-L15.

[7] Li. Y. and Oldenburg, D.W. (1998). "3-D inversion of gravity data." Geophysics, Vol. 63, PP. 109-119.

[8] Boulanger, O. and Chouteau, M. (2001). "Constraints in 3D gravity inversion." Geophysical Prospecting, Vol. 49, No. 2, PP. 265– 280.

[9] Portniaguine, O. and Zhdanov, M.S. (2002). "3-D magnetic inversion with data compression and image focusing." Geophysics, Vol. 67, PP. 1532–1541.

[10] Chasseriau, P. and Chouteau, M. (2003). "3D gravity inversion using a model of parameter covariance." Journal of Applied Geophysics, Vol. 52, No. 1, PP. 59-74.

[11] Caratori Tontini, F., Cocchi, L. and Carmisciano, C. (2006). "Depth-to-the-bottom optimization for magnetic data inversion: Magnetic structure of the Latium volcanic region, Italy." Journal of Geophysical Research, Vol. 111, PP. 1-17.

[12] Pignatelli, A., Nicolosi, I. and Chiappini, M. (2006). "An alternative 3D source inversion method for magnetic anomalies with depth resolution." Annals of Geophysics, Vol. 49, PP. 1021-1027.

[13] Malehmir, A., Thunehed, H. and Tryggvason, A. (2009). "A Case History: the Paleoproterozoic Kristineberg mining area, northern Sweden: Results from integrated 3D geophysical and geologic modeling, and implications for targeting ore deposits." Geophysics, Vol. 74, PP. B9-B22.

[14] Namaki, L., Gholami, A. and Hafizi, M.K. (2011). "Edge-preserved 2-D inversion of magnetic data: an application to the Makran arc-trench complex." Geophysical Journal International, Vol. 184, No. 3, PP. 1058-1068.

[15] Shamsipour, P., Chouteau, M. and Marcotte, D. (2011). "3D stochastic inversion of magnetic data." Journal of Applied Geophysics, Vol. 73, No. 4, PP. 336-347.

[16] Cella, F. and Fedi, M. (2012). "Inversion of potential field data using the structural index as weighting function rate decay." Geophysical Prospecting, Vol. 60, No. 2, PP. 313-336.

[17] Li, Y. and Oldenburg, D.W. (2003). "Fast inversion of large-scale magnetic data using wavelet transforms and a logarithmic barrier method." Geophysical Journal International, Vol. 152, No. 2, PP. 251-265.

[18] Charbonnier, P., Blanc-Feraud, L., Aubert, G. and Barlaud, M. (1997). "Deterministic edge-reserving regularization in computed imaging." IEEE Transactions on Image Processing, Vol. 6, PP. 298–310.

[19] Geman, S. and McClure, D.E. (1985). "Bayesian image analysis: an application to single photon emission tomography, in Proc. Statistical Computation Section." PP. 12–18, Amer. Statistical Assoc., Washington, DC.

[20] Sacchi, M.D. and Ulrych, T.J. (1995). "High resolution velocity gathers and offset space reconstruction." Geophysics, Vol. 60, PP. 1169-1177.

[21] Bertete-Aguirre, H., Cherkaev, E. and Oristaglio, M. (2002). "Non-smooth gravity problem with total variation penalization functional." Geophysical Journal International, Vol. 149, No. 2, PP. 499–507.

[22] Farquharson, C.G. (2008). "Constructing piecewise-constant models in multidimensional minimum-structure inversions." Geophysics, Vol. 73, No. 1, PP. K1-K9.

[23] Gholami, A. and Siahkoohi, H.R. (2009). "Simultaneous constraining of model and data smoothness for regularization of geophysical inverse problems." Geophysical Journal International, Vol. 176, No. 1, PP. 151–163.

[24] Abedi, M., Gholami, A. and Norouzi, G.H. (2013). "A stable downward continuation of airborne magnetic data: A case study for mineral prospectivity mapping in Central Iran." Computers & Geosciences, Vol. 52, PP. 269–280.

[25] Abedi, M., Mosazadeh, K., Dehghani, H. and MadanchiZare, A. (2014). "Enhancing magnetic signals in unexploded ordnances (UXO) detection based on edge-preserved stable downward continuation method." Journal of Mining & Environment, Vol. 5, No. 1, PP. 13-24.

[26] Routh, P.S., Qu, L., Sen, M.K. and Anno, P.D. (2007). "Inversion for nonsmooth models with physical bounds." SEG, Expanded Abstracts, Vol. 26, No. 1, PP. 1795–1799.

[27] Donoho, D.L. (1995). "Nonlinear solution of linear inverse problems by wavelet-vaguelette decomposition." Applied and Computational Harmonic Analysis, Vol. 2, No. 2, PP. 101–126.

[28] Donoho, D.L. and Johnsstone, I.M. (1998). "Minmax estimation via wavelet shrinkage." Annals of Statistics, Vol. 26, PP. 879-921.

[29] Daubechies, I., Defriese, M. and De Mol, C. (2004). "An iterative thresholding algorithm for linear inverse problems with a sparsity constraint." *Communications* on *Pure and Applied Mathematics, Vol.* LVII, PP. 1413–1457.

[30] Loris, I., Nolet, G., Daubechies, I. and Dahlen, F.A. (2007). "Tomographic inversion using l1-norm regularization of wavelet coefficients." Geophysical Journal International, Vol. 170, PP. 359–370.

[31] Lelièvre, P.G. and Oldenburg, D.W. (2009). "A 3D total magnetization inversion applicable when significant, complicated remanence is present." Geophysics, Vol. 74, No. 3, PP. L21-L30.

[32] Li, Y., Shearer, S.E., Haney, M.M. and Dannemiller, N. (2010). "Comperhensive approaches to 3D inversion of magnetic data affected by remanent magnetization." Geophysics, Vol. 75, PP. L1-L11.

[33] Bhattacharyya, B.K. (1964). "Magnetic anomalies due to prism-shaped bodies with arbitrary polarization." Geophysics, Vol. 29, PP. 517–53.

[34] Rao, D.B. and Babu, N.R. (1991). "A rapid method for three-dimensional modeling of magnetic anomalies." Geophysics, Vol. 56, PP. 1729-1737.

[35] Daubechies, I. (1988). "Orthonormal bases of compactly supported wavelets." *Communications* on *Pure and Applied Mathematics,* Vol. 41, PP. 909-996.

[36] Aster, R.C., Borchers, B. and Thurber, C. (2003). "Parameter Estimation and Inverse Problems." Academic Press, New York, NY.

[37] Bregman, L. (1967). "The relaxation method of finding the common points of convex sets and its application to the solution of problems in convex optimization." USSR Computational Mathematics and Mathematical Physics, Vol. 7, PP. 200–217.

[38] Donoho, D.L. (1995). "De-noising by soft thresholding." IEEE Transactions on Information Theory, Vol. 41, PP. 613–627.

[39] Daubechies, I. (1992). "Ten Lectures on Wavelets". SIAM, Philadelphia.

[40] Mallat, S.G. (1998). "A Wavelet Tour of Signal Processing". Academic Press, San Diego.

[41] Li, Y. and Oldenburg, D.W. (2000). "Joint inversion of surface and three-component borehole magnetic data." Geophysics, Vol. 65, PP. 540-552.

[42] Elyasi, G.R. (2009). "Mineral Potential Mapping in Detailed Stage Using GIS in One of Exploration Prospects of Kerman Province." Master of Science Thesis, University of Tehran (published in Persian).

[43] Clark, D.A. (1999). "Magnetic petrology of igneous intrusions-Implications for exploration and magnetic interpretation." Exploration Geophysics, Vol. 20, PP. 5–26.

[44] John, D.A., Ayuso, R.A., Barton, M.D., Blakely, R.J., Bodnar, R.J., Dilles, J.H., Gray, Floyd, Graybeal, F.T., Mars, J.C., McPhee, D.K., Seal, R.R., Taylor, R.D. and Vikre, P.G. (2010). "Porphyry copper deposit model, chap. B of Mineral deposit models for resource assessment." U.S. Geological Survey Scientific Investigations Report 2010–5070–B, PP. 169.

[45] Thoman, M.W., Zonge, K.L. and Liu, D. (2000). "Geophysical case history of North Silver Bell, Pima County, Arizona—A supergene-enriched porphyry copper deposit, in Ellis RB, Irvine R, Fritz F, eds., Northwest Mining Association 1998 Practical Geophysics Short Course Selected Papers on CD-ROM: Spokane, Washington. Northwest Mining Association, paper 4, PP. 42.

[46] Oldenburg, D.W., Li, Y. and Ellis, R.G. (1997). "Inversion of geophysical data over a copper gold porphyry deposit: A case history for Mt. Milligan." Geophysics, Vol. 62, PP. 1419-1431.

[47] Telford, W.M., Geldart, L.P. and Sheriff, R.E. (2004). "Applied Geophysics". Second Edition, Cambridge University Press.

[48] Hezarkhani, A. (2009). "Hydrothermal fluid geochemistry at the Chah-Firuzeh porphyry copper deposit, Iran, evidence from fluid inclusions." Journal of Geochemical Exploration, Vol. 101, No. 3, 254–264.